nature communications

Article

https://doi.org/10.1038/s41467-024-53846-6

Breaking dielectric dilemma via polymer functionalized perovskite piezocomposite with large current density output

Received: 12 January 2024

Accepted: 23 October 2024

Published online: 04 November 2024

Check for updates

Asif Abdullah Khan[1,2,7], Avi Mathur[2,3,7], Lu Yin[2,4], Mahmoud Almadhoun[2], Jian Yin[1,2], Majid Haji Bagheri[1,2], Md Fahim Al Fattah[1,2], Araz Rajabi-Abhari[5], Ning Yan[5], Boxin Zhao[2,4], Vivek Maheshwari[2,3] ✉ & Dayan Ban[1,2,6] ✉

Organometal halide perovskite (OHP) composites are flexible and easy to synthesize, making them ideal for ambient mechanical energy harvesting. Yet, the output current density from the piezoelectric nanogenerators (PENGs) remains orders of magnitude lower than their ceramic counterparts. In prior composites, high permittivity nanoparticles enhance the dielectric constant (ϵ_r) but reduce the dielectric strength (E_b). This guides our design: increase the dielectric constant by the high ϵ_r nanoparticle while enhancing the E_b by optimizing the perovskite structure. Therefore, we chemically functionalize the nanoparticles to suppress their electrically triggered ion migration for an improved piezoelectric response. The polystyrene functionalizes with $FAPbBr_2I$ enlarges the grains, homogenizes the halide ions, and maintains their structural integrity inside a polymer. Consequently, the PENG produces a current density of 2.6 $\mu Acm^{-2}N^{-1}$. The intercalated electrodes boost the current density to 25 $\mu Acm^{-2}N^{-1}$, an order of magnitude enhancement for OHP composites, and higher than ceramic composites.

Piezoelectric nanogenerators use the piezoelectric effect for harnessing ambient vibrations to trickle charging modern electronic devices and sensing networks. Due to their unique merits in compact size, weight, and stability in harsh environments, PENGs are considered one of the most suitable energy harvesting technologies in recent years to be used with wearable, flexible, and implantable sensing platforms. Piezoceramics such as $Pb(ZrTi)O_3$ (PZT)[1], $BaTiO_3$ (BTO)[2,3], Pb $(Zn_{1/3}Nb_{2/3})O_3$-$PbTiO_3$ (PZN-PT)[4], Sm-$Pb(Mg_{1/3}Nb_{2/3})O_3$-$PbTiO_3$ (Sm-PMN-PT)[5] are the dominant materials of choice for PENG applications due to their large piezoelectric charge constants. Yet, their brittle nature and cost pose challenges in various applications. Consequently, flexible polymers like poly (vinylidene fluoride) (PVDF)[6,7], poly(vinylidene fluoride-co-trifluoro ethylene) (PVDF-TrFE)[8], polydimethylsiloxane (PDMS)[9], etc. are used as host matrices in conjunction with piezoceramic fillers.

The successful utilization of PENG as an energy source hinges on attaining both sufficiently high voltage and current outputs. While the output voltage from PENG exceeds 3 V (sufficient for most charging applications), a significant challenge in addressing the charging needs of most electronic devices persists in their low output current densities. Diverse strategies have been implemented to boost current densities, including the exploration of innovative device structures and the selection of materials with high piezoelectric charge constant (d_{33}). For instance, by stacking PZT NW arrays Gu et al. fabricated PENG

[1]Department of Electrical and Computer Engineering, University of Waterloo, 200 University Ave west, Waterloo N2L 3G1 ON, Canada. [2]Waterloo Institute for Nanotechnology, University of Waterloo, 200 University Ave West, Waterloo N2L 3G1 ON, Canada. [3]Department of Chemistry, University of Waterloo, 200 University Ave West, Waterloo N2L 3G1 ON, Canada. [4]Department of Chemical Engineering, University of Waterloo, 200 University Ave West, Waterloo N2L 3G1 ON, Canada. [5]Department of Chemical Engineering and Applied Chemistry, University of Toronto, 200 College Street Toronto, Ontario, ON, Canada. [6]School of Physics and Electronics, Henan University, No. 1 Jinming street, Kaifeng, Henan, P. R. China. [7]These authors contributed equally: Asif Abdullah Khan, Avi Mathur. ✉e-mail: vmaheshwari@uwaterloo.ca; dban@uwaterloo.ca

with a current density of 23 μAcm^{-2} in 2013[10], in 2014, Park et al. developed PZT thin film-based PENG with interdigitated electrodes and reported a current density of 150 μAcm^{-2} [11]. Materials with high piezoelectric charge constants yield high output current density in a PENG while reducing the piezoelectric voltage coefficient (g_{33}) and the output voltage according to the relation of ($g_{33} = d_{33}/\varepsilon_r$; ε_r is the relative permittivity). However, if the high d_{33} ceramic material is dispersed in a high g_{33} polymer matrix such as PVDF, PVDF-TrFE, it can yield a high output current density while retaining a standard output voltage level above 3 V. For instance, Sm-PMN-PT@PVDF piezoceramic composite has a current density of 15 μAcm^{-2} (1.24 μAcm^{-2}N^{-1}), and a voltage of 7 V. In 2020, Gu et al. marked another record of output current density to 290 μAcm^{-2} (24 μAcm^{-2}N^{-1}) by stacking 72-layers of Sm-PMN-PT@PVDF films, which is still the best-reported piezoceramic composite[7]. The critical metric for assessing the PENG performance lies in the normalized current density, denoted in μAcm^{-2}N^{-1}. This parameter considers the applied force necessary for the generation of the reported current, offering a comprehensive gauge of the device's operational efficiency.

Organometal halide perovskites (OHPs) are currently a focal point of extensive research for their application in PENG devices[12–16]. This interest is driven by multiple advantages, including their solution processability, flexibility, and low-temperature synthesis when compared to traditional piezoceramics. These features enable the fabrication of OHP-based PENG devices on large-area flexible substrates, making them suitable for applications in flexible, wearable, and implantable electronics. Recent research has demonstrated that the piezoelectric charge constants (d_{33}) of OHPs are now comparable to those of piezoceramics. For example, TMCM-$MnCl_3$ (TMCM, trimethylchloromethyl ammonium) (d_{33} ~185 pCN^{-1}), TMCM-$CdCl_3$ (d_{33} ~220 pCN^{-1})[17], $(TMFM)_x(TMCM)_{1-x}$-$CdCl_3$ (TMFM, tri-methyl fluoromethyl ammonium; $0 \le x \le 1$) (d_{33} ~1540 pCN^{-1})[18], etc. Despite the use of high piezoelectric charge constant OHPs, the challenge of achieving high current density persists. For instance, the maximum current density for the TMCM-$CdCl_3$@PDMS composite was reported as 3.45 μAcm^{-2} (equivalent to 0.69 μAcm^{-2} N^{-1})[19].

Like piezoceramics, a prevalent strategy to improve the performance of OHP-based PENGs (and others) involves utilizing a matrix of piezoelectric polymers such as PVDF in combination with OHP nanomaterial. Poling in such composites induces the formation of the electroactive β-phase through electrostatic interaction with the nanomaterial[20]. Despite achieving hundreds of volts in output voltage[21], the normalized current density of such PENGs remains notably low, with the highest reported value at 0.72 μAcm^{-2}N^{-1} [13]. This figure is roughly 30 times lower than the best-performing PENGs utilizing piezoceramics. A challenge in such composites arises from the trade-off between achieving a high dielectric constant and their low dielectric strength. While a high dielectric constant enhances polarization (resulting in a higher piezoelectric charge constant), the lower dielectric strength limits the poling of these composites at sufficiently high electric fields for extended durations[22]. Consequently, the unidirectional alignment of piezoelectric domains cannot be achieved, compromising optimal performance. In the case of OHPs, the breakdown is induced by ion migration effects under the applied poling electric field, leading to perovskite structure degradation. Grain boundaries play a critical role as preferred pathways for ion migration. Due to the higher electrical conductivity of OHPs, they act as current pathways, and alterations to their structure, such as the formation of PbI_2 or local p-n junctions, reduce conductivity and, consequently, current density in the PENGs.

In this study, we present a $FAPbBr_2I$-PVDF-based PENG where polystyrene (PS) is employed to control the structure and compositional variation of $FAPbBr_2I$. This ternary piezocomposite in a PENG generates a high output current density of 11 μAcm^{-2} (2.6 μAcm^{-2}N^{-1}). The piezocomposites were further used as a building block to vertically assemble them. The multiple layers of piezocomposite films separated through intercalated copper electrodes enhance the output current density. The cascade-type piezoelectric nanogenerator (CPENG) architecture (14 layers) exhibits an impressive output current density of approximately 105 μAcm^{-2} (peak to peak) at 30 Hz and 4.2 N, with a corresponding normalized current density of 25 μAcm^{-2}N^{-1}. This performance surpasses OHP-based PENGs by an order of magnitude and outperforms the best ceramic-based composites, as reported with a normalized current density of 24.17 μAcm^{-2}N^{-1} in a 72-layer PENG. The basis of this improvement is due to (1) The use of PS leads to improved grain size which reduces the density of grain boundaries, as a result, ion migration is reduced by an order of magnitude compared to plain $FAPbBr_2I$-PVDF. (2) With the use of PS, a uniform distribution of halide ions (Br^- and I^-) is achieved in the composite, this leads to a homogenous band structure and prevents the formation of local energy barriers (due to variation in band structure from changes in halide composition) which could impede current collection. (3) The dielectric constant of the PS-$FAPbBr_2I$-PVDF composite is improved by over five times compared to plain $FAPbBr_2I$-PVDF, which will increase the piezoelectric charge constant. (4) X-ray diffraction results reveal increased lattice spacing with the use of PS, indicating strain relaxation in the OHP structure. This further reduces ion migration, improves carrier mobility, and lowers defect concentration, contributing to the stabilization of the PENG devices and enhancing charge collection[23]. These effects collectively contribute to a higher breakdown strength in PS-$FAPbBr_2I$-PVDF-based PENGs, sustaining up to 30 min of poling at a field strength of ~50 Vμm^{-1} compared to plain $FAPbBr_2I$-PVDF devices that typically breakdown in less than 1 min under similar conditions. Thus, our work demonstrates the successful mitigation of challenges associated with OHP-based piezoelectric nanogenerators through a synergistic approach involving optimized material design and effective device engineering by cascading multiple layers. This integrated strategy achieves a record-normalized current density.

Results and discussion

Design and characterization of polymer functionalized perovskite composites

Polystyrene was used to functionalize the OHP ($FAPbBr_2I$) because of its specific interactions with, the A site cation (FA^+) and the lead halide species. Additionally, its high dielectric strength, along with low dielectric losses[24], makes it particularly advantageous for PENG applications. Previous studies have demonstrated that integrating PS into the perovskite matrix results in the modulation of both nucleation and the growth rate of perovskite crystal grains, accompanied by a reduction in defect density[25]. The functionalization is grounded in the typical cation-π interaction between the FA^+ cation of the $FAPbBr_2I$ and π -electrons of aromatic styrene in PS, as illustrated in Fig. 1a. The specific molecular-level interaction between perovskite precursor and PS was characterized by Raman spectroscopy (Fig. S1). The pristine $FAPbBr_2I$-PVDF and PS-$FAPbBr_2I$-PVDF films exhibit sharp characteristic peaks of Pb–X (X = I, Br) lattice mode centered at 80 cm^{-1} and a broad peak (160–250 cm^{-1}) corresponding to the organic moiety[26]. As observed in Fig. 1b, adding 1 wt/vol% PS in the $FAPbBr_2I$, the peak corresponding to the Pb–X (X = I, Br) lattice mode shifts to a lower wavenumber. Such variation in the Raman active modes of the perovskite signifies an enhanced molecular-level interaction between PS and perovskite precursors. A similar interaction between PS and the organometal halide perovskite precursors has been previously

https://doi.org/10.1038/s41467-024-53846-6

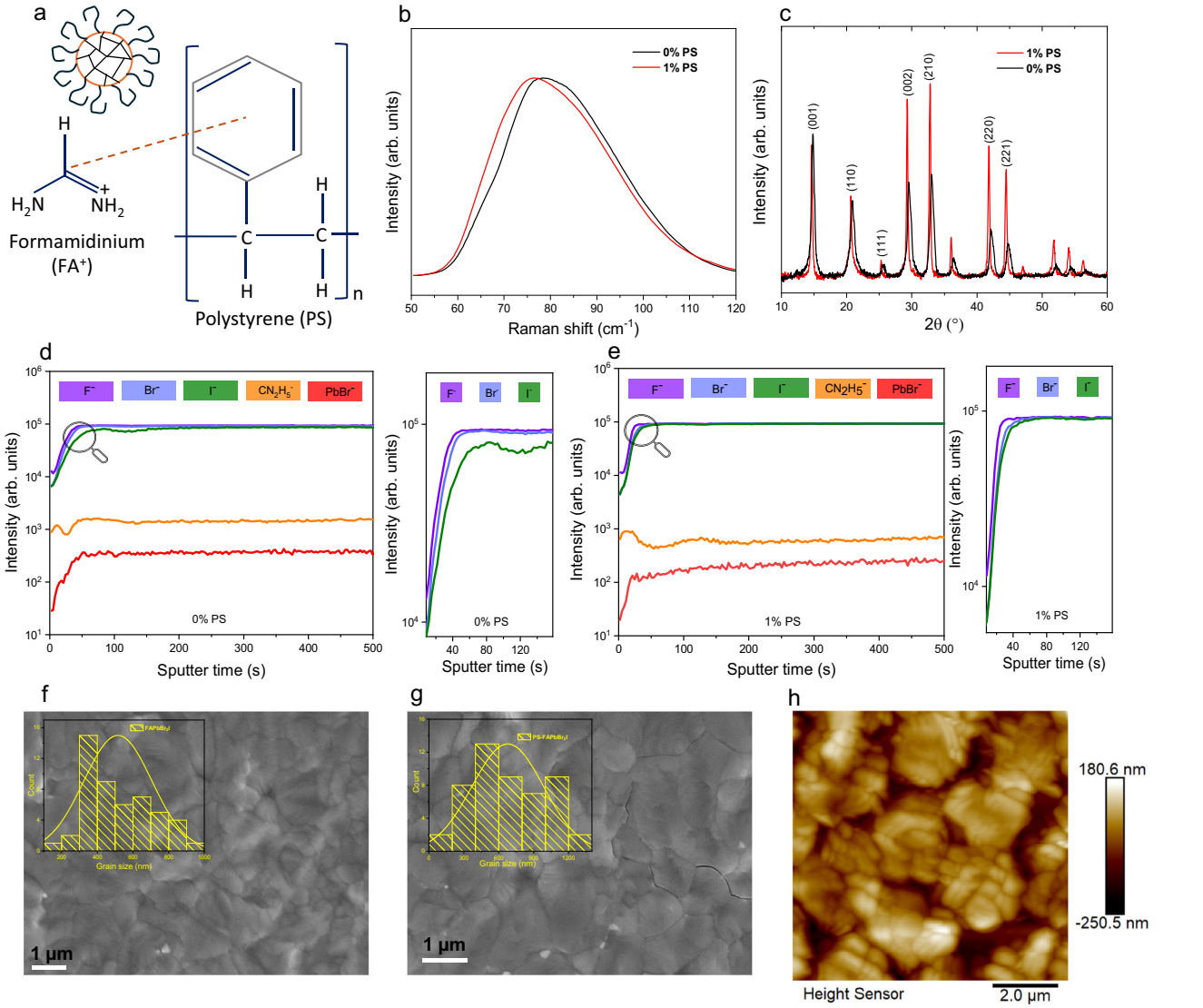

Fig. 1 | Surface functionalization of organometal halide perovskite. a Cation−π interaction mechanism between $FAPbBr_2I$ and the PS. **b** Raman spectroscopy and **c** XRD patterns of the pristine $FAPbBr_2I$-PVDF and 1% PS-$FAPbBr_2I$-PVDF films. **d** ToF-SIMS depth profiling of pristine and **e** 1% PS-$FAPbBr_2I$-PVDF films. **f** FE-SEM images of the grains of plain $FAPbBr_2I$ and **g** 1% PS-functionalized $FAPbBr_2I$ thin film (insets show the grain size distribution curves). **h** AFM surface topography image of the 1% PS-$FAPbBr_2I$ film. Source data are provided as a Source Data file.

confirmed by gel permeation chromatography and the growth of single crystal perovskite[27]. The X-ray diffraction pattern in Fig. 1c shows the presence of the dominant peaks corresponding to (0 0 1) (0 0 2) and (2 1 0) lattice planes and highlights the formation of the mixed halide perovskite phase in both pristine $FAPbBr_2I$-PVDF and PS-$FAPbBr_2I$-PVDF films[28,29]. A stronger anisotropic orientation along the (0 0 1) plane is evident in pristine $FAPbBr_2I$ compared to PS-$FAPbBr_2I$. From the view of thermodynamics, orientation diversity offers increased entropy and a more stable perovskite phase[30]. The narrowing of the peak (reduction in the full width and half maximum value) and increase in the peak intensity in the PS-$FAPbBr_2I$-PVDF XRD pattern indicates improved crystallinity and an increase in the crystallite size (Tables S1, S2)[31]. An additional shoulder peak of residual PbX_2 (X = I, Br) is observed at 2θ of 12.4 ° exclusively in the pristine $FAPbBr_2I$. The absence of the PbX_2 (X = I, Br) peak in the PS-perovskite composite film can be ascribed to the ability of PS chains to interact with PbI_2 and $PbBr_2$, which are weak Lewis acids and formed intermittently during solvation of perovskite precursors. This leads to enhanced perovskite phase conversion from the combined interaction between PS, FA, and PbX_2. Additionally, there is a consistent shift in the XRD peaks toward lower 2θ values in PS-$FAPbBr_2I$-PVDF films compared to $FAPbBr_2I$-PVDF films. This shift indicates a lattice expansion in the PS-$FAPbBr_2I$-PVDF films, signifying relaxation in the perovskite lattice[32]. The lattice constants calculated from the peak positions in the XRD pattern further illustrate this expansion (Tables S3, S4 and Note S1).

Time-of-flight secondary ion mass spectroscopy (ToF-SIMS) depth profiling (Fig. 1d, e) was conducted to see the variation in the distribution of the halide ions between PS-$FAPbBr_2I$-PVDF and $FAPbBr_2I$ -PVDF films. We observe that a uniform concentration of I^- and Br^- is present across the PS-$FAPbBr_2I$-PVDF composite film. In comparison, for the $FAPbBr_2I$-PVDF film, the I^- distribution is lower and non-uniform (especially during the initial 0–200 s of sputtering) relative to the Br^- profile, hence showing phase segregation in the top layer. Phase segregation of the halide ions can lead to detrimental effects on the device's performance due to structural changes[33]. In the perovskite solution system, the atoms, ions, and solvent molecules can coordinate with each other, forming intermediate adducts or complexes. Since the trend of Lewis acidity in lead (II) halide follows the order of $PbI_2 > PbBr_2$, the stronger interaction of PbI_2 with PS allows more iodide-rich perovskite phase

formation, which leads to its uniform distribution across the film[34]. This observation, combined with the shift of the peak position in the X-ray diffraction patterns for PS-FAPbBr$_2$I-PVDF, confirms that the perovskite lattice is larger due to the uniform inclusion of the higher ionic radii of the 6-coordinated I^- (r_{I^-} = 2.06 Å) along with Br^- (r_{Br^-} = 1.82 Å). The larger lattice will also have a smaller strain which has been shown to improve the stability of the perovskite phase, along with decreased defect density and increased carrier mobility[35,36]. The depth profiling data also reveals that the signal intensity of the I^- ion is maintained at the same level as that of the F^- ion (representative of PVDF) across the entire depth of the sputtering time (Fig. 1d) in the PS-FAPbBr$_2$I-PVDF film. This shows that the composite is homogenous, and the interaction between PVDF and the perovskite phase will be uniform across the film.

The direct interaction of PS chains with the perovskite precursors leads to relatively larger grain size in the PS-FAPbBr$_2$I films in comparison to that of pristine FAPbBr$_2$I as evident in the lateral field emission scanning electron microscopy images (Fig. 1f, g). Due to the decreased nucleation rate, average grain sizes increase from 400 to 600 nm (in FAPbBr$_2$I) to 600–900 nm in the PS-FAPbBr$_2$I film. The distribution curve in Fig. 1f, g represents the probability density function at each of the values in x using the normal distribution with mean μ and standard deviation σ. The corresponding equation is given by:

$$f(x\,|\mu,\sigma) = \frac{1}{\sigma\sqrt{2\pi}} e^{\frac{-(x-\mu)^2}{2\sigma^2}}$$

The AFM surface topology (Fig. 1h) also confirms the large grain formation on the PS-functionalized film. Therefore, based on these combined effects we expect greater stability of the perovskite phase in the PS-FAPbBr$_2$I-PVDF films, along with lower ion migration effects.

Dielectric and piezoelectric properties of the piezocomposite

An electric field was applied across the composite film to align the dipoles unidirectionally to generate a macroscopic dipole moment. The electric field applied for a sufficiently longer time causes 60/180° rotation of the molecular chains and a conversion of the α to the β-phase even without the mechanical stretching of the chains[37]. The most widely used PVDF polymer requires a high electric field of at least 50 Vμm^{-1} to completely harness its piezoelectric capabilities[38]. Such a requirement imposes serious restrictions in manipulating OHP composites, as a high electric field proliferates dynamic point defects and causes faster breakdown due to ion migration, as illustrated in Fig. 2a. In an OHP perovskite structure, FA^+, Br/I^-, and Pb^{2+} are all considered mobile ions, and this results in high ionic conductivity, and a large leakage current in the perovskite-based devices[31,39,40]. We find that, with an external bias in the dark, an electronic current is instantly observed owing to the fast movement of the electronic charge carriers. At the same time, the mobile ions with low activation energy also slowly drift toward metal electrodes. As the oppositely charged ions begin accumulating at the metal electrodes, the ion-induced electric field partially cancels the external bias and reduces the overall current. This transient decay in current is observed until the ion accumulation reaches an equilibrium condition (Fig. 2b). The pristine FAPbBr$_2$I film owing to the higher density of mobile ionic defects and halide ion segregation exhibits a large decay in the current[41]. As seen in Fig. 2b, the dark current in the pristine FAPbBr$_2$I film decays rapidly from its initial value of 3.10×10^{-6} and reaches 1.86×10^{-6} mA/cm^2 (~40% decay) within 35 s. In contrast, the PS-FAPbBr$_2$I films exhibit a much lower dark current (~5.0×10^{-7} mA/cm^2) which decays by a smaller magnitude to ~4.20×10^{-7} mA/cm^2. The smaller magnitude of decay in the dark current implies that the PS reduces the ion migration effect by more than an order of magnitude, based on the structural results discussed above. Furthermore, the electric field strength-dependent leakage current density[42] of pure FAPbBr$_2$I-PVDF-based devices is observed to be 5.44×10^{-4} mA/cm^2 at 0.1 kV/cm and 1.49×10^{-2} mA/cm^2 at 3 kV/cm (Fig. S2). In contrast, the leakage currents in the 1 wt% PS-FAPbBr$_2$I-PVDF composite films are reduced to 1.67×10^{-5} and 1.35×10^{-3} mA/cm^2, respectively, at the same electric fields. The multiple-fold reduction in the leakage current in the presence of PS further corroborates its beneficial role in providing insulation against the leakage paths in the composite film while simultaneously allowing improved grain growth and homogenized distribution of FAPbBr$_2$I nanoparticles across the PVDF matrix.

The structural integrity of the OHP perovskite in the composite is crucial to preventing undesirable breakdown during poling. We compared the average dielectric strength of 12 different locations on each of the composite devices (Experimental data in Table S5). The 1% PS devices had an average breakdown strength of 191 Vμm^{-1}, 130% times that of the films without PS (Fig. S3). Based on the average poling electric field of composites being between 40 and 120 Vμm^{-1}, we applied a dc bias of 3 kV to the pristine (without any PS) and 1% PS-containing composites (thickness of ~ 65 and ~58 μm, respectively in Fig. S4) and noted the breakdown time (Fig. 3a)[38]. With the electric field of ~46 Vμm^{-1}, all the pristine films reached their breakdown point in less than 5 min, while 50% of them could withstand only 1 min of poling. In contrast, the PS-containing composites could survive up to 30 min of poling with an electric field of ~51 Vμm^{-1}, where the lowest-performing devices have a breakdown point higher than all the pristine composite samples.

A striking difference was observed in the relative dielectric permittivity (ϵ_r) of the plain, and PS-functionalized composite films. In contrast to the ϵ_r of 7.5 in pristine FAPbBr$_2$I, the 1% PS-functionalized films exhibit a ϵ_r value of 38 (Fig. 3b), representing an increase of more than five times. The more homogeneous distribution of perovskite species and improved crystallinity with larger grain size are anticipated to increase the dielectric constant of 1% PS composites (Note S2)[43]. Since grain boundaries typically have smaller dielectric permittivity than the grains in perovskite materials[44,45]. The observed peak shift to smaller angles in the XRD data suggests a relaxation in the perovskite lattice. This relaxation is also expected to enhance dipole alignment and polarizability[46].

We varied the PS concentration and observed its influence on the output current generation in the PENG devices. The output current density from the PENG devices improved, especially for the 1% PS-containing FAPbBr$_2$I film, which has the highest current density of 11 μA/cm^2. This is 2.4 times higher than the pristine perovskite PENGs, and 7.3 times higher than pristine PVDF-based devices (Fig. 3c). This is attributed to the structural effects which include larger grain size, defect passivation of perovskites, and enhanced dielectric constant with a more homogenous composition of the composite[47,48]. The interaction between PS-FAPbBr$_2$I and PVDF was studied from the absorbance spectra of pure PS, pure PVDF, PVDF-PS, and PVDF-PS-FAPbBr$_2$I films (Fig. S5). In the FTIR spectra (Fig. S5a), the characteristic peaks of PS appear at 696 cm^{-1} (aromatic ring bending), 1492 cm^{-1} (aromatic ring mode), 2850 and 2923 cm^{-1} (CH_2 symmetric and asymmetric stretching), and 3025, 3059, and 3081 cm^{-1} (aromatic C-H stretching). Similarly, distinctive peaks of PVDF centered at 487 cm^{-1} (CF_2 bending and wagging), 613 cm^{-1} (CF_2 bending and CCC skeletal vibration), 763 cm^{-1} (CH_2 and CF_2 in-plane rocking or bending), 875 cm^{-1} (CC symmetric stretching and skeletal bending) and 1184 cm^{-1} (CF_2 stretching) are observed[49,50].

In the PVDF-PS film, the characteristics peaks for PVDF show no change which indicates little interaction between PS and PVDF. The intensity of PS-related peaks is reduced due to its minimal concentration (1 wt%). In the PS-FAPbBr$_2$I-PVDF film, while the peaks observed in the PVDF-PS film are retained, a new peak corresponding to the CN stretching in the formamidinium group of perovskite appears at 1715 cm^{-1}. Furthermore, the IR peak corresponding to CC

https://doi.org/10.1038/s41467-024-53846-6

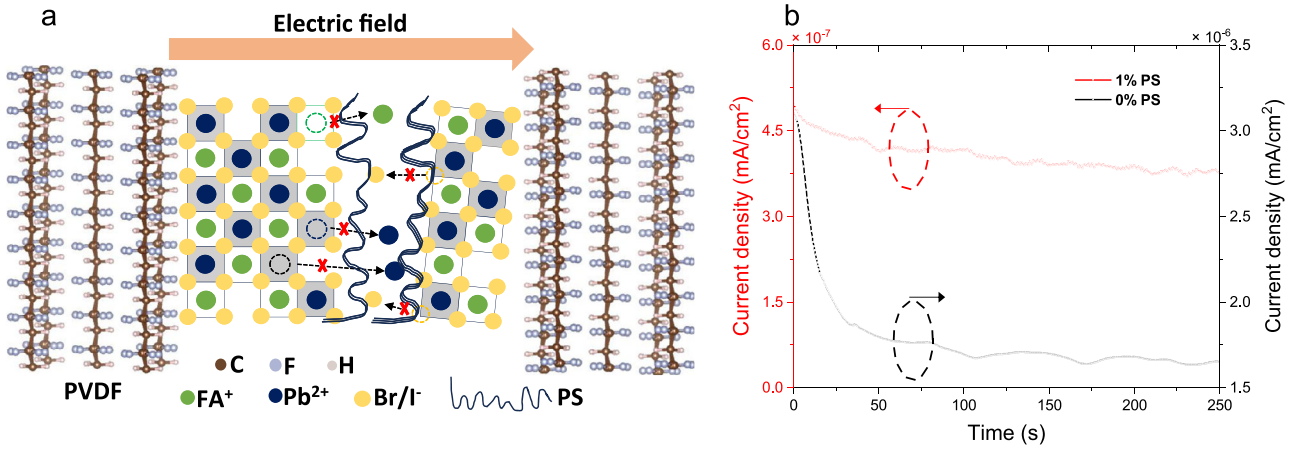

Fig. 2 | Electric-field induced Ion-migration in an OHP composite film. **a** Schematic representation of ion-migration mechanism and role of the PS in a $FAPbBr_2I$-PVDF composite film. The arrows indicate the direction of ion migration, while the red cross symbols represent the PS chains blocking the ion migration paths. **b** The dark-current density of pristine and 1% PS-functionalized composites. Source data are provided as a Source Data file.

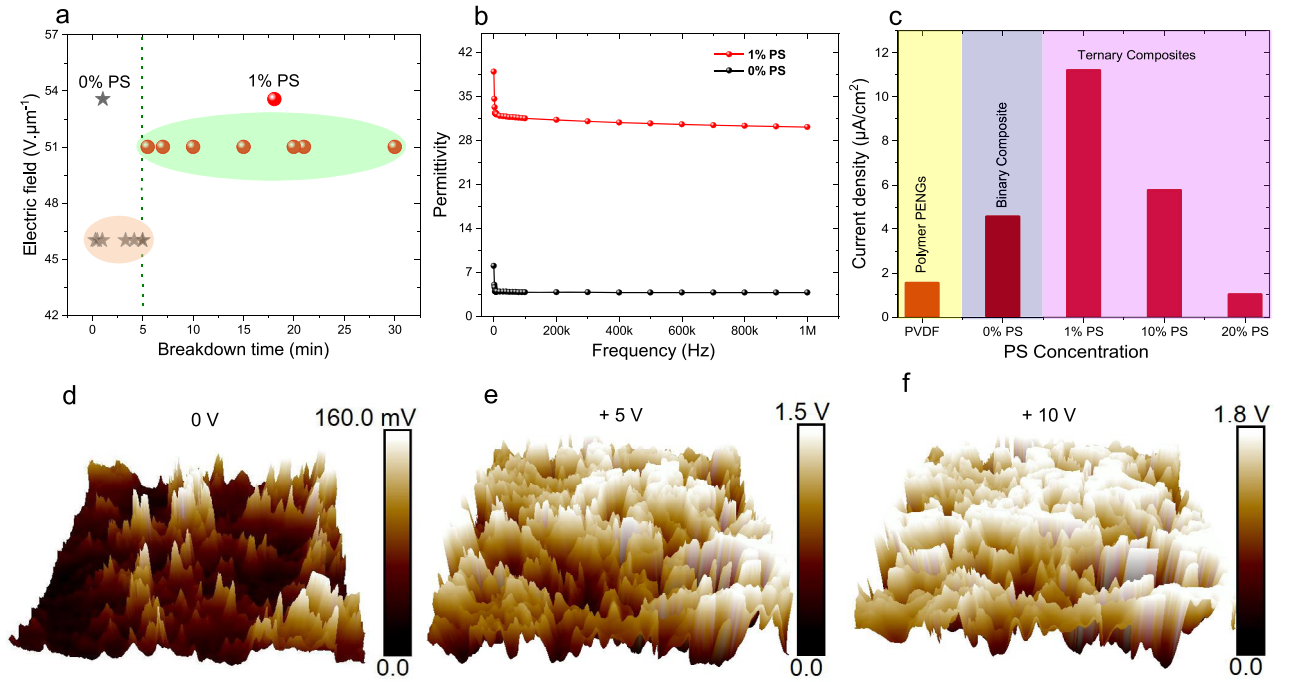

Fig. 3 | Piezoelectric and dielectric response of the OHP composite film. **a** Variation of electrical breakdown time of the pristine and 1% PS included composites of $FAPbBr_2I$-PVDF with an applied electric bias of 3 kV. The red-shaded region represents the composite films without PS, while the green-shaded region corresponds to the composite films containing 1% PS. **b** Measured permittivity (ϵ_r) of the composites. **c** Output current density of the PENGs fabricated with varying PS concentration. **d**–**f** 3D representation (NanoScope Analysis 1.8) of the piezoelectric response in a 1% PS-$FAPbBr_2I$-PVDF film with different tip biases (area of $2 \times 2\ \mu m^2$). Source data are provided as a Source Data file.

stretching in PVDF shifts from 875 cm^{-1} to a higher wavenumber of 880 cm^{-1} indicating interaction with the perovskite (Fig. S5b). The critical feature is that with PS-OHP in the PVDF matrix, the β-phase content in PVDF increases from 36 to 71.5%. This is based on the diminishing of the α-phase PVDF peaks at 614, 763, and 974 cm^{-1} in the PS-PVDF-Perovskite film. An enhancement in the relative intensity of the IR peaks at 840 and 1276 cm^{-1} is observed which correspond exclusively to the β-phase of PVDF[51]. Nevertheless, at higher PS concentrations, effective perovskite content reduces in the film, and this decreases the overall film quality and the effective beta-phase amount in the PVDF. So, a decreasing trend in output current density with larger PS loading is observed (Fig. S6). The output voltage from the 0% PS film is slightly lower than the 1% PS film, while PS loading beyond 1% further decreases the output voltage (Fig. S7). To assess its flexibility[52], Young's modulus (YM) of the composites with different PS additions was also measured from the tensile stress-strain curves (Fig. S8). The Young's modulus was calculated for the 0% PS film as 1.35 GPa, while for the 1 and 10% PS-added films it was reduced to 1.3 and 1.16 GPa. Thus, obtaining a delicate balance with the amount of PS in the composite is critical. We measured the microscopic piezoelectric response with the applied electric bias (+5 V, +10 V) in a piezoelectric force microscopy (PFM) (Fig. 3d–f). The 1% PS

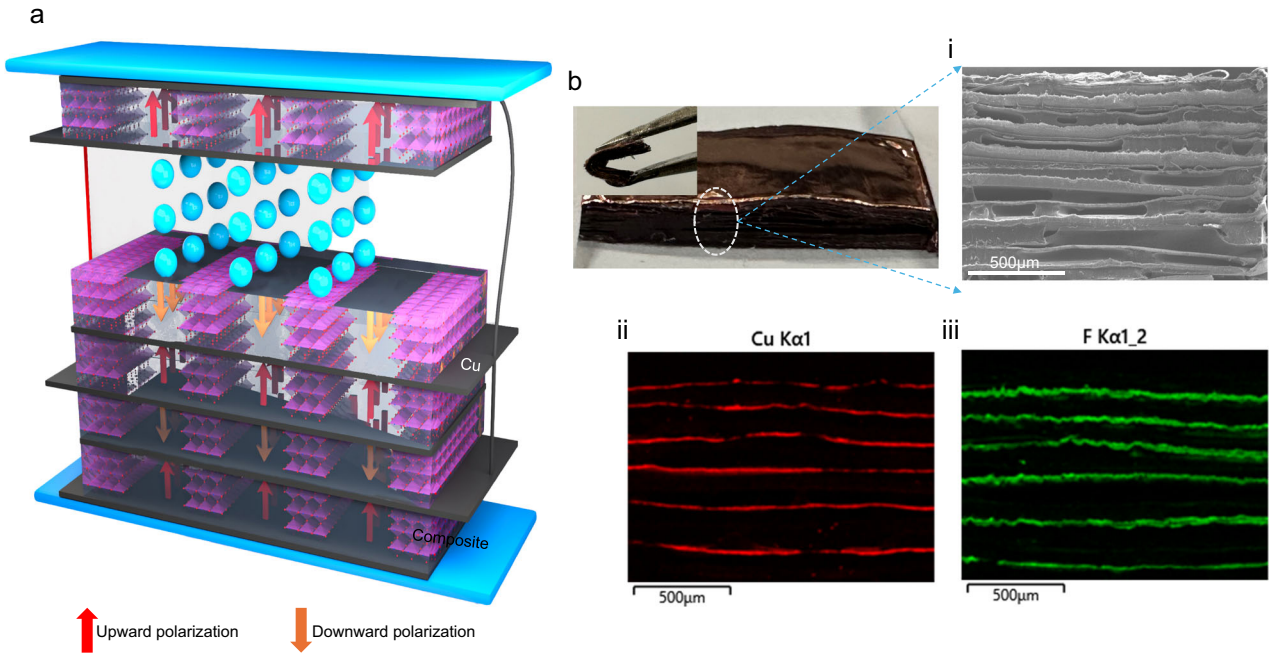

Fig. 4 | Design of the cascade-type piezoelectric nanogenerator (CPENG). a The basic structure of the CPENG. The blue spheres represent the repeating composite films, while the polyhedral shapes depict the perovskite structure embedded in the PVDF. Each of the composites is connected in parallel electrical connection. Two consecutive films have opposite polarization directions and are intercalated with a copper electrode. Intercalated electrodes adjacent to the same polarization direction are connected. **b** Photograph of a 21-layer CPENG (inset shows a bent device by a metallic tweezer) (i) cross-sectional FE-SEM (ii-iii) EDS elemental mapping clearly showing the intercalated copper electrodes (red) and composite films (green).

composite film poled with +5 V dc bias for ~10 min exhibits an amplitude response of ~1.5 V, which is ~10 times more than the non-poled film (0 V). As we increased the dc bias to +10 V for 10 min, amplitude response further increased to ~1.8 V. It is evident that with the rise in electrical poling voltage and poling time, more and more dipoles are unidirectionally aligned and resulting in a higher piezoelectric response in the composite film. This experiment further depicts the importance of electrical poling of the composite film for obtaining an enhanced piezoelectric response.

Design of the CPENG

The enhanced current density and stability observed in the 1% PS composites served as motivation to adopt it as a foundational element for the assembly of the multilayer cascade-type piezoelectric nanogenerator (CPENG). In a PENG, the piezoelectric polarization charges are utilized to produce output current to the external circuit. When subjected to mechanical stress, opposite polarization charges emerge at the interfaces of the top and bottom electrodes. The prospect of creating numerous interfaces through two-dimensional electrodes within a piezoelectric film holds the potential for an enhancement in output current density[53]. To achieve this cascade device, we employed intercalated copper electrodes positioned between two oppositely poled composite films (Fig. 4a). The electrodes were interconnected in a parallel electrical configuration, where positive polarization surfaces were linked to create a common positive (+ve) terminal, and the negative surfaces of the films formed a shared negative (−ve) terminal. When subjected to force, the current generated in each unit accumulated through the interfacial electrodes, resulting in a larger combined current output. A solvent-free urethane-based prepolymer was employed as an adhesive owing to its outstanding initial adhesion, workability, and bonding capacity[54]. Briefly, the adhesive was blend-coated on a thin copper electrode and tightly pressed with the composite film for 48–72 h in ambient conditions. Subsequently, another composite with opposite polarity was coated with adhesive and securely bonded to the copper electrode, forming a single-electrode intercalated two-layer PENG device (further details can be found in the Experimental section). This process was repeated to fabricate CPENGs with 1, 4, 8, 14, and 21 layers. Figure 4b presents a photograph of a CPENG with 21 layers, accompanied by cross-sectional scanning electron microscopy images and cross-section images obtained through energy-dispersive X-ray spectroscopy (EDS) analysis. The elemental mapping images corresponding to copper (Fig. 4b-ii) and fluorine (Fig. 4b-iii) illustrate the copper electrodes and PVDF composite films, respectively. Other representative elements of the perovskite (Pb, Br, I, and N) from the EDS analysis are also shown in Fig. S9. This represents the homogeneous distribution of perovskite nanoparticles within the piezocomposite and well-intercalated copper electrodes between the composite films.

We conducted a mechanistic investigation using finite element analysis to understand how the assembly of multiple layers could optimize the output performance (Fig. S10). We simulated the piezo potential of various models with 1, 4, 8, 14, and 21 layers of films, maintaining opposite polarization directions for two consecutive films. With an increase in the number of layers, the piezo potential decreases from 30 V (single layer) to 3 V for a 21-layer PENG. When a force is applied to the PENG, the dipole moments become smaller along the thickness direction, leading to the cancellation of the piezo potential due to the opposite polarization direction of two consecutive films[55]. However, the change in polarization across each layer translates to output current, which is then multiplied through intercalated electrodes.

Output performance and application of the CPENG

To assess the practical mechanical energy harvesting capabilities of the devices, we applied a force of 4.2 N (0.42 kg) using a steel block and systematically examined their respective performance. The single-layer PENG produced a maximum output voltage of approximately 29 V. This voltage gradually decreased to 17, 7, 3.5, and 2.6 V for the 4,

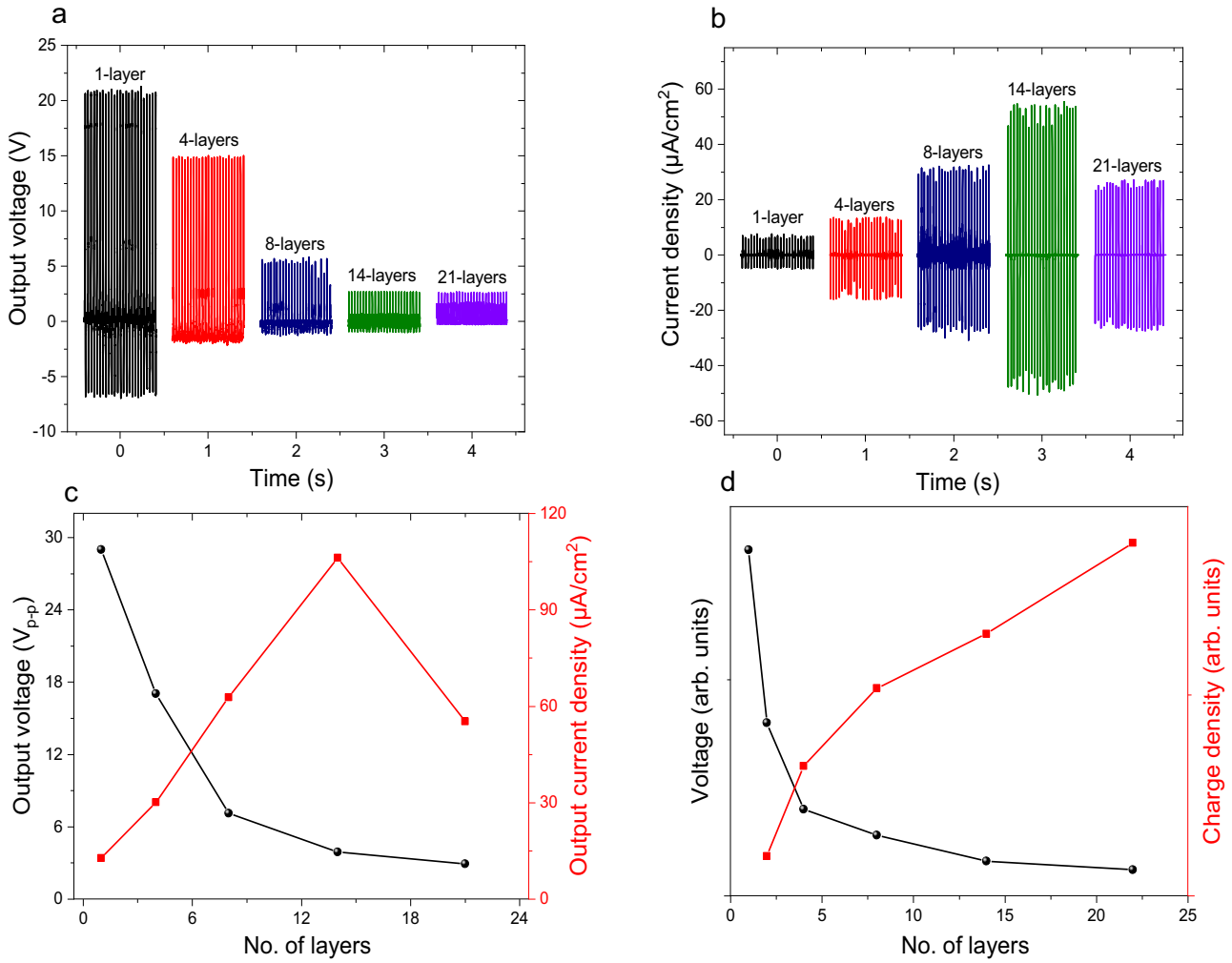

Fig. 5 | Output performance of the CPENGs. a Measured output voltage and **b** current density of CPENGs made with 1, 4, 8, 14, and 21 layers. Comparison of experimental (**c**) and simulated (**d**) variation of output voltage and current density with total number of layers. Source data are provided as a Source Data file.

8, 14, and 21-layer devices, respectively (Fig. 5a). This behavior can be elucidated through the simple capacitor model, wherein the parallel connection of capacitors leads to an increase in overall capacitance, subsequently causing a decrease in voltage (V = Q/C; V voltage, Q charge, and C capacitance)[56].

The output current density of the devices was measured under short-circuit conditions, as illustrated in Fig. 5b. As the number of layers increased to 1, 4, 8, 14, and 21, the output current density rose from 11 to 29 μA/cm², 64, 105, and then decreased to 55 μA/cm², respectively. Figure 5c demonstrates that while the output voltage decreases nonlinearly, the output current density increases almost linearly with the number of layers. Moreover, the finite element simulation model reveals that the calculated total charge density in short-circuit conditions (which corresponds to current density) follows a similar increasing trend with the number of layers in a PENG, as depicted in Fig. 5d. The simulation results in Fig. 5d align with our experimental findings, except for the current density for the 21-layer CPENG. This is due to the strong stress-buffering effect as the number of layers increases[7]. The use of a higher number of copper/adhesive electrodes will reduce the transmitted stress to each composite, which was not included in the simulation model[57,58].

The CPENG demonstrated resilience during testing for ~1000 mechanical cycles without deterioration in its performance, as shown in Fig. S11. To validate its practical energy harvesting capabilities, we connected the CPENG through a full bridge rectifier to different capacitors (Fig. 6a). The CPENG was used to charge different capacitors of 4.7, 10, 22, and 47 μF (Fig. 6b). At 30 Hz and 4.2, N it can charge a 4.7 μF capacitor to ~1 V in 16 s, 10 μF to 1 V in 38 s, 22 μF to 0.95 V in 50 s, and 47 μF to 0.6 V in 1 min.

Gently triggering it with a finger generated and stored electricity, with 24 touches charging a 1 μF capacitor to 0.8 V, showcasing a high charging rate for a PENG at low frequency (Fig. S12). Additionally, the CPENG (four layers) powered a System on Chip (SoC) at 30 Hz (Fig. 6c), enabling it to activate a radio frequency (RF) transmitter module embedded in the SoC every 2 min.

It's worth emphasizing that the defect-passivated composite films developed in this work can be scaled up for more practical applications. We normalized the output current density of the 14-layer CPENG with the applied force of 4.2 N and compared it with state-of-the-art PENGs (Fig. 6d). The output current density per unit force in the CPENG is notably higher, surpassing the reported OHP-based PENGs by an order of magnitude. Among ceramic-based composites, the 72-layer PENG holds the highest reported normalized current density of 24.17 $\mu Acm^{-2}N^{-1}$. In contrast, the 14-layer CPENG in this study, with PS-$FAPbBr_2I$ composites, generates 25 $\mu Acm^{-2}N^{-1}$. This finding underscores that the normalized current density of the PS-functionalized perovskite composite system in this work is the best-reported among PENG devices (Table S6). We anticipate that this discovery further underscores the economic and technological advantages of using organometal halide perovskites over ceramic piezoelectrics in PENG

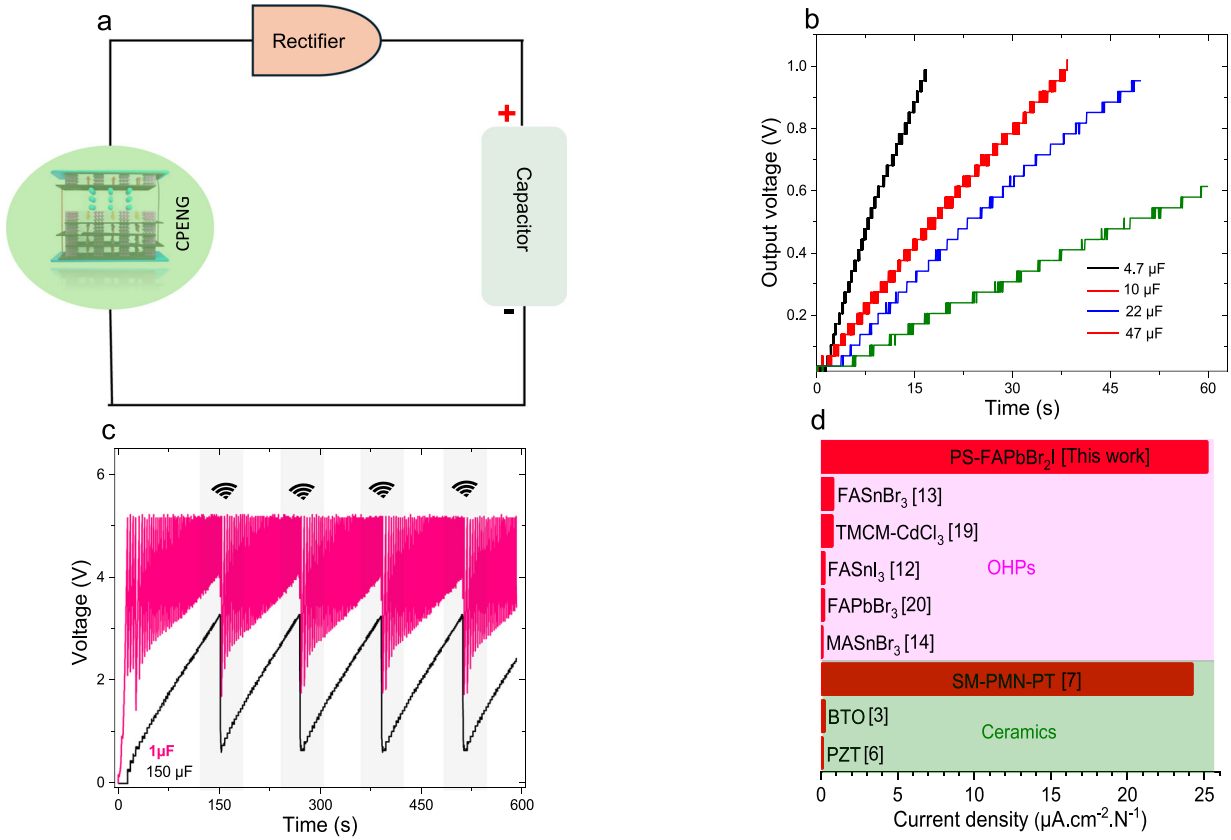

Fig. 6 | Application of the CPENG. a Schematic of an electrical circuit for energy storing to a capacitor. **b** Mechanical energy is converted to electrical energy by the CPENG to charge different capacitors. **c** The CPENG is charging an LTC 3588-2 system on a chip (SoC). **d** Comparison of normalized current density with CPENG and other representative PENGs. Source data are provided as a Source Data file.

applications and will pave the way for new developments to enhance the performance of PENG-based devices.

In summary, the innovative approach of functionalizing organometal halide perovskite with polystyrene has been successfully employed to enhance the output current density of the piezoelectric nanogenerator. The optimization of polystyrene concentration in $FAPbBr_2I$ precursors has been instrumental in reducing defects, increasing grain size, and achieving a more homogeneous distribution of halide ions, resulting in a smaller lattice strain. Consequently, the PS-functionalized organometal halide perovskite (PS-OHP) exhibits greater structural integrity, reducing ion migration under an electric field and overcoming the "dielectric constant vs. dielectric strength" limit. The optimized concentration of 1% PS significantly suppresses leakage current by one order of magnitude, demonstrating effective control over ion migration. Additionally, the controlled nucleation of perovskites through PS incorporation leads to a twofold increase in grain sizes compared to pristine perovskites. This innovative ternary composite design and cascading them help to elevate the output current density of the extensively studied perovskite PENG by one order of magnitude thus setting a record. The high-performance PENG with ultrahigh current density achieved in this study represents a stride towards establishing a sustainable power source for portable and flexible electronics.

Methods

Synthesis of the pristine and PS-$FAPbBr_2I$ precursor solution

The $FAPbBr_2I$ precursor solution was prepared by dissolving an equimolar ratio (0.5: 0.5) of FAI (formamidinium iodide ≥99%, Sigma-Aldrich) and $PbBr_2$ (lead(ii)bromide ≥98%, Sigma-Aldrich) in an *N*, *N*-DMF (*N*, *N*-dimethylformamide ≥99%, Sigma-Aldrich) solvent, followed by stirring at 60 °C for 12 h. To prepare PS-$FAPbBr_2I$ precursor solutions of varying concentration (1, 5, 10, and 20 wt./vol%), a corresponding amount of PS (average Mw 35 kDa, Sigma-Aldrich) was added to the perovskite precursor solution and stirred for 30 min.

Synthesis of the PS-$FAPbBr_2I$-PVDF composites

The PVDF solution was dissolved in *N*, *N* DMF with constant stirring at 50 °C for 24 h. The final concentration of the PVDF in DMF was kept at 10 wt%. Then, the PS-$FAPbBr_2I$-PVDF composite precursor solutions were prepared by homogeneously mixing 1 wt/vol% PS-$FAPbBr_2I$ and 10 wt% PVDF. To optimize the concentration, the 1, 10, and 20 wt/vol% composite solutions were synthesized. Then the mixed solution was drop-cast onto a glass substrate and stored for ~1 h for the degassing process, immediately followed by annealing at 120 °C. Highly crystalline composite films were obtained after 2 hours. Distributed nanoparticles with an average diameter of 15–20 nm inside the PVDF matrix were estimated by the high-resolution TEM image in Fig. S13a. Selected area electron diffraction (SAED) of the nanoparticles observed in the TEM were also shown in Fig. S13b, c. To align the dipoles in the PS-$FAPbBr_2I$-PVDF film, high-voltage electrical poling was completed with an electric field of 50–120 $V\mu m^{-1}$ for 2–3 h. After poling, the films were sandwiched between two copper electrodes. To prepare the electrodes, commercially available copper foil sheets with a thickness and resistance of 2.5 μm, and 0.05 Ω/cm^2 were used. The copper sheets were cleaned with acetone, isopropanol, and deionized water to remove any adhesives on them. Then the prepared copper sheets were

dried with nitrogen and cut into small sizes (1 cm × 0.45 cm) for use in the PENGs. Finally, the sandwiched structure of the polyester/copper/PS-FAPbBr$_2$I-PVDF/copper/polyester film was pressed through thermal lamination, which eliminates air gaps and provides uniform adhesion between the copper electrodes and the piezoelectric film. Before poling, output current density was measured as 0.51 μA cm^{-2}, compared to 11 μA cm^{-2} after the poling (Fig. S14). When we switched the terminals of the poled PENG, the measured output current density signal also switched, indicating the signal originating from the inherent piezoelectricity of the composite film (Fig. S15).

Multilayer assembly of the PS-FAPbBr$_2$I-PVDF composites

Each of the poled composite films was cut into 1.3 cm × 0.6 cm dimensions. Solvent-free urethane-based prepolymer was used as an adhesive between the electrode and the composite film. First, a few drops of the urethane prepolymer were poured on the copper electrode and spread with a glass rod to achieve uniformity. Second, the composite film was pressed tightly on the copper for adhesion. Third, another copper electrode was attached to the top of the composite film by using step one. Fourth, a few drops of urethane prepolymer were poured on another composite film and spread uniformly with a glass rod. Fifth, the composite film was pressed tightly on the copper electrode of step 3. Sixth, step 1 was repeated to grow the top copper electrode. In this way, two units of the composite films were cascaded. Then, steps 4, 5, and 6 were repeated to assemble 14 different layers. The polarity (polarization direction) of the composite films was determined by the electrical poling direction. Between two consecutive films, opposite polarity was maintained. Electrodes at the positive interfaces were shorted to make a single positive terminal, and similarly, electrodes of the negative interfaces were shorted to make a single negative terminal for the electrical measurements. The fabricated device can be bent by using a metallic tweezer (Fig. S16). However, the stiffness will gradually increase with the number of layers. All the devices are characterized in compression mode. Finally, the device was packaged in between thermal laminating pouches.

Structural, microscopic, and spectroscopic characterization

The X-ray diffraction characterization was carried out on the PANalytical Empyrean diffractometer with Cu Kα radiation (λ = 1.54 Å). A Zeiss Ultraplus field emission scanning electron microscopy (FE-SEM) was utilized for visualizing the surface topology and grain size distribution of the pristine and polymer-integrated perovskite films. The Raman spectroscopy for all films was performed using a Horiba HR800 spectrometer at an excitation wavelength of 532 nm and 6 mW power in the backscattering configuration. The time-of-flight second ion mass spectroscopy (ToF-SIMS) was performed to analyze depth profiling of freshly prepared perovskite and polymer-perovskite films using Cs^+ ion source (500 eV) for sputtering and Bi^{3+} (30 keV) for analysis over ToF-SIMS 5, ION-ToF GmbH. Transmission electron microscopy (TEM) was recorded by using a Hitachi HT7700 transmission electron microscope with an acceleration voltage of about 100 kV. FTIR absorbance spectra were collected by using Nicolet iS50 (Thermo Fisher Scientific).

Dielectric measurements

The dielectric constant was measured by using a Keithley-4200 semiconductor parameter analyzer. An ac bias voltage of 100 mV was applied, while the frequency was swept from 0 to 1 MHz. We measured the capacitances by using parallel plate capacitor model approximation to calculate the dielectric constant. Dielectric strength was measured by applying voltage from a high-voltage DC source on the top copper electrodes of the composite films. We increased the applied voltage with a step size of 500 V. All the experiments were conducted in the ambiance.

Electrical and mechanical measurements

The dark current measurement on the planar vertical device configuration was conducted using a probing station in a two-probe mode. A Keysight 6614C 50-watt system power supply was used for applying an external bias and the current was measured using a Keysight 3458A Digital multimeter. The perovskite film was connected in series with the multimeter and power supply to complete the circuit. Piezoelectric force microscopy was conducted by a Bruker AFM (Dimension Icon) in a vertical PFM mode. The probe used for the PFM was a n-doped (antimony) silicon coated with reflecting platinum (Pt)/ iridium (Ir) on the back and had a nominal stiffness of 3 N/m. Data analysis, including 3D representations of the PFM images was performed by using NanoScope Analysis 1.8. To study the electrical output performance of the PENGs an electrodynamic shaker (Lab Works Inc.) was used, controlled by a power amplifier and a controller. A digital oscilloscope (Tektronix 2004 C) and a low-noise current preamplifier (SR 570, Stanford Research Systems Inc.) were used to measure the electrical signal output from the nanogenerators. A 10X signal cable was used to collect the voltage signals from the PENGs. Young's modulus (YM) of the composite films was measured from the tensile stress-strain curves obtained by an Instron 5548 micro tester.

Data availability

The data supporting this study, and its Supplementary Information are available within the paper. Additional information is available from the corresponding authors, D.B. and V.M., upon request. Source data are provided with this paper (ref. 59). Source data are provided with this paper.

References

1. Jaffe, B., Roth, R. S. & Marzullo, S. Piezoelectric properties of Lead zirconate-Lead titanate solid-solution ceramics. *J. Appl. Phys.* **25**, 809–810 (1954).
2. Park, K. L. et al. Piezoelectric $BaTiO_3$ thin film nanogenerator on plastic substrates. *Nano Lett.* **10**, 4939–4943 (2010).
3. Jian, G. et al. 3D $BaTiO_3$ flower based polymer composites exhibiting excellent piezoelectric energy harvesting properties. *Adv. Mater. Interfaces* **7**, 2000484 (2020).
4. Park, S. E. & Shrout, T. R. Ultrahigh strain and piezoelectric behavior in relaxor based ferroelectric single crystals. *J. Appl. Phys.* **82**, 1804–1811 (1997).
5. Li, F. et al. Ultrahigh piezoelectricity in ferroelectric ceramics by design. *Nat. Mater.* **17**, 349–354 (2018).
6. Hong, Y. et al. Hierarchically interconnected piezoceramic textile with a balanced performance in piezoelectricity, flexibility, toughness, and air permeability. *Adv. Funct. Mater.* **31**, 2104737 (2021).
7. Gu, L. et al. Enhancing the current density of a piezoelectric nanogenerator using a three-dimensional intercalation electrode. *Nat. Commun.* **11**, 1030 (2020).
8. Liu, Y. et al. Ferroelectric polymers exhibiting behaviour reminiscent of a morphotropic phase boundary. *Nature* **562**, 96–100 (2018).
9. Zhou, Z. et al. Interface modulated 0-D piezoceramic nanoparticles/PDMS based piezoelectric composites for highly efficient energy harvesting application. *Nano Energy* **82**, 105709 (2021).
10. Gu, L. et al. Flexible fiber nanogenerator with 209 V output voltage directly powers a light-emitting diode. *Nano Lett.* **13**, 91–94 (2012).
11. Park, K. L. et al. Highly-efficient, flexible piezoelectric PZT thin film nanogenerator on plastic substrates. *Adv. Mater.* **26**, 2514–2520 (2014).
12. Pandey, R. et al. Microscopic origin of piezoelectricity in lead-free halide perovskite: application in nanogenerator design. *ACS Energy Lett.* **4**, 1004–1011 (2019).

13. Rana, M. M. et al. Enhanced piezoelectricity in lead-free halide perovskite nanocomposite for self-powered wireless electronics. *Nano Energy* **101**, 107631 (2022).
14. Ippili, S., Jella, V., Kim, J., Hong, S. & Yoon, S. G. Unveiling predominant air-stable organotin bromide perovskite toward mechanical energy harvesting. *ACS Appl. Mater. Interfaces* **12**, 16469–16480 (2020).
15. Jella, V. et al. A comprehensive review of flexible piezoelectric generators based on organic-inorganic metal halide perovskites. *Nano Energy* **57**, 74–93 (2019).
16. Liu, J. et al. Giant piezoelectric output and stability enhancement in piezopolymer composites with liquid metal nanofillers. *Adv. Sci.* **10**, 2304096 (2023).
17. You, Y.-M. et al. An organic-inorganic perovskite ferroelectric with large piezoelectric response. *Science* **357**, 306–309 (2017).
18. Liao, W.-Q. et al. A molecular perovskite solid solution with piezoelectricity stronger than lead zirconate titanate. *Science* **363**, 1206–1210 (2019).
19. Gong, Y. J. et al. High power density energy harvesting and human motion monitoring with [trimethyl chloromethyl ammonium] [$CdCl_3$]/polymer composite. *Matter* **6**, 2066–2080 (2023).
20. Ding, R. et al. High-performance piezoelectric nanogenerators composed of formamidinium lead halide perovskite nanoparticles and poly(vinylidene fluoride). *Nano Energy* **37**, 126–135 (2017).
21. Khan, A. A. et al. Maximizing piezoelectricity by self-assembled highly porous perovskite-polymer composite films to enable the internet of things. *J. Mater. Chem. A* **8**, 13619–13629 (2020).
22. Huang, Y. et al. Enhanced piezoelectricity from highly polarizable oriented amorphous fractions in biaxially oriented poly(vinylidene fluoride) with pure β crystals. *Nat. Commun.* **12**, 675 (2021).
23. Ghosh, D. et al. Lattice expansion in hybrid perovskites: effect on optoelectronic properties and charge carrier dynamics. *J. Phys. Chem. Lett.* **10**, 5000–5007 (2019).
24. Guan, F. et al. Confined ferroelectric properties in poly(vinylidene fluoride-co- chlorotrifluoroethylene)-graft-polystyrene graft copolymers for electric energy storage applications. *Adv. Funct. Mater.* **21**, 3176–3188 (2011).
25. Mathur, A., Li, A. & Maheshwari, V. Nanoscale architecture of polymer–organolead halide perovskite films and the effect of polymer chain mobility on device performance. *J. Phys. Chem. Lett.* **12**, 1481–1489 (2021).
26. Kontos, A. G. et al. Halogen–NH_2^+ interaction, temperature-induced phase transition, and ordering in $(NH_2CHNH_2)PbX_3$ (X = Cl, Br, I) hybrid perovskites. *J. Phys. Chem. C.* **124**, 8479–8487 (2020).
27. Saraf, R., Mathur, A. & Maheshwari, V. Polymer-controlled growth and wrapping of perovskite single crystals leading to better device stability and performance. *ACS Appl. Mater. Interfaces* **12**, 25011–25019 (2020).
28. Touré, A., Bouich, A., Soucasse, B. M. & Soro, D. Investigation of the optoelectronics properties and stability of Formamidinium lead mixed halides perovskite. *Opt. Mater.* **135**, 113334 (2023).
29. Kim, S. et al. High-power and flexible indoor solar cells via controlled growth of perovskite using a greener antisolvent. *ACS Appl. Energy Mater.* **3**, 6995–7003 (2020).
30. Zhang, S. et al. Controlling orientation diversity of mixed ion perovskites: reduced crystal microstrain and improved structural stability. *J. Phys. Chem. Lett.* **10**, 2898–2903 (2019).
31. Zhang, B. B. et al. Defect proliferation in $CsPbBr_3$ crystal induced by ion migration. *Appl. Phys. Lett.* **116**, 063505 (2020).
32. Pengpad, A. et al. Surface composition of MAPb (I_x $Br_{1-x)3}$ (0≤x≤1) organic-inorganic mixed-halide perovskites. *Appl. Surf. Sci.* **479**, 311–317 (2019).
33. Knight, A. J. et al. Halide segregation in mixed-halide perovskites: influence of A-site cations. *ACS Energy Lett.* **6**, 799–808 (2021).
34. Wharf, H., Gram, T., Ad, S. T., Makhija, R. & Onyszchuk, M. Synthesis and vibrational spectra of some lead (II) halide adducts with O-, S-, and N-donor atom ligands. *Can. J. Chem.* **54**, 3439–3452 (1976).
35. Kim, G. et al. Impact of strain relaxation on performance of α-formamidinium lead iodide perovskite solar cells. *Science* **370**, 108–112 (2020).
36. Rehman, W. et al. Charge-carrier dynamics and mobilities in formamidinium lead mixed-halide perovskites. *Adv. Mater.* **27**, 7938–7944 (2015).
37. Ramos, M. M. D., Correia, H. M. G. & Lanceros-Méndez, S. Atomistic modelling of processes involved in poling of PVDF. *Comput. Mater. Sci.* **33**, 230–236 (2005).
38. Jiang, F. & Lee, P. S. Performance optimization strategies of halide perovskite-based mechanical energy harvesters. *Nanoscale Horiz.* **7**, 1029–1046 (2022).
39. Walsh, A. & Stranks, S. D. Taking control of ion transport in halide perovskite solar cells. *ACS Energy Lett.* **3**, 1983–1990 (2018).
40. Wei, D. et al. Ion-migration inhibition by the cation–π interaction in perovskite materials for efficient and stable perovskite solar cells. *Adv. Mater.* **30**, 1707583 (2018).
41. Bae, S. et al. Electric-field-induced degradation of methylammonium lead iodide perovskite solar cells. *J. Phys. Chem. Lett.* **7**, 3091–3096 (2016).
42. Kim, J. et al. High permittivity $CaCu_3Ti_4O_{12}$ particle-induced internal polarization amplification for high performance triboelectric nanogenerators. *Adv. Energy Mater.* **10**, 1903524 (2020).
43. Lee, E. J. et al. High-performance piezoelectric nanogenerators based on chemically-reinforced composites. *Energy Environ. Sci.* **11**, 1425–1430 (2018).
44. Ihlefeld, J. F. et al. Scaling effects in perovskite ferroelectrics: fundamental limits and process-structure-property relations. *J. Am. Ceram. Soc.* **99**, 2537–2557 (2016).
45. Minussi, F. B., Reis, S. P. & Araújo, E. B. Effects of frequency, temperature, and dc bias electric field on the dielectric properties of methylammonium lead iodide from the perspective of a relaxor-like ferroelectric. *Acta Mater.* **219**, 117235 (2021).
46. Anusca, I. et al. Dielectric response: answer to many questions in the methylammonium lead halide solar cell absorbers. *Adv. Energy Mater.* **7**, 1700600 (2017).
47. Tong, W. et al. Enhanced electricity generation and tunable preservation in porous polymeric materials via coupled piezoelectric and dielectric processes. *Adv. Mater.* **32**, 2003087 (2020).
48. Liu, H. et al. Greatly enhanced energy density in polymer nanocomposites coated with high-k perovskite nanosheets. *Mater. Today Energy* **31**, 101213 (2023).
49. Chipara, D. et al. Spectroscopic investigations on PVDF-Fe_2O_3 nanocomposites. *J. Appl. Polym. Sci.* **137**, 48907 (2020).
50. Lanceros-Méndez, S., Mano, J. F., Costa, A. M. & Schmidt, V. H. FTIR and DSC studies of mechanically deformed β-PVDF films. *J. Macromol. Sci.* **40 B**, 517–527 (2001).
51. Gregorio, R. & Cestari, M. Effect of crystallization temperature on the crystalline phase content and morphology of poly(vinylidene fluoride). *J. Polym. Sci. B Polym. Phys.* **32**, 859–870 (1994).
52. Kim, J. et al. Triboelectric nanogenerators for battery-free wireless sensor system using multi-degree of freedom vibration. *Adv. Mater. Technol.* **9**, 2301427 (2024).
53. Jin, D. W. et al. Polarization- and electrode-optimized polyvinylidene fluoride films for harsh environmental piezoelectric nanogenerator applications. *Small* **17**, 2007289 (2021).
54. Jing, T. et al. Highly stretchable, high efficiency room temperature self-healing polyurethane adhesive based on hydrogen bonds-

applicable to solid rocket propellants. *Polym. Chem.* **12**, 4532–4545 (2021).
55. Yan, M. et al. Enhanced energy harvesting performance in lead-free multi-layer piezoelectric composites with a highly aligned pore structure. *Nano Energy* **106**, 108096 (2023).
56. Yu, X. et al. Boosting output current density of piezoceramic energy harvesters using three-dimensional embedded electrodes. *Nano Energy* **101**, 107598 (2022).
57. Huo, Z. Y. et al. Triboelectrification induced self-powered microbial disinfection using nanowire-enhanced localized electric field. *Nat. Commun.* **12**, 3693 (2021).
58. Hinchet, R. et al. Transcutaneous ultrasound energy harvesting using capacitive triboelectric technology. *Science* **365**, 491–494 (2019).
59. Khan, A. A. et al. Polymer functionalized perovskite piezo-composites with large current density output data sets. xlsx. figshare https://doi.org/10.6084/m9.figshare.27091777 (2024).

Acknowledgements

This work was supported by the Natural Science and Engineering Research Council of Canada (no. RGPIN-2022-03161 to D.B.). The authors thank the Quantum-Nanofabrication & Characterization Facility (QNFCF), and Giga-to-Nanoelectronics Center (G2N), University of Waterloo for the experiment facilities.

Author contributions

A.A.K. and A.M. contributed equally to this work. A.A.K. and A.M. conceived and designed the study, performed experiments, and conducted data analysis and interpretation, with contributions from L.Y., M.A., J.Y., M.H.B., M.F.A.F., A.R., N.Y., and B.Z.A. A.K. and A.M. drafted the initial manuscript with input from all authors. All authors participated in result discussions and contributed to the final manuscript. D.B. and V.M. jointly supervised the work.

Competing interests

The authors declare no competing interests.

Additional information

Supplementary information The online version contains supplementary material available at https://doi.org/10.1038/s41467-024-53846-6.

Correspondence and requests for materials should be addressed to Vivek Maheshwari or Dayan Ban.

Peer review information *Nature Communications* thanks Dengwei Hu, Sang-Woo Kim, Soon-Gil Yoon and the other, anonymous, reviewer(s) for their contribution to the peer review of this work. A peer review file is available.